Progress In Electromagnetics Research C, Vol. 132, 129–144, 2023

A Novel Low Profile Turbinella Shaped Antenna for 5G Millimeter Wave Applications

Madhusudhanan Nair Ayyappan*, Abhijeet Gaonkar, and Pragati Patel

Abstract—This article investigates a Turbinella-shaped super wideband monopole antenna designed to accommodate the attributes of the fifth-generation (5G) technology which is the enhanced Mobile Broadband (eMBB). The antenna is designed to work with the current millimetre wave bands, including n77, n78, and n258, and it provides the increased data rate needed for eMBB applications. The proposed antenna comprises a Turbinella-shaped patch, a 50 Ω tapered feed line, and a multi-slotted partial ground plane. The self-similarity and space-filling nature of circular geometrical fractal is employed in a novel way to acquire antenna compactness and broadband performances. Further with the design of a tuning fork-shaped Defective Ground Structure (DGS), super wideband characteristics to incorporate 5G millimeter bands are obtained. The proposed antenna has a compact size of $0.25\lambda \times 0.32\lambda$ along with a bandwidth of 173.33% along the frequency ranging from 3 to 41.97 GHz and has achieved a compactness of 81%. Moreover, the fundamental dimension limit theorem is used to demonstrate the antenna's compactness. Time domain analysis is also studied in this article.

1. INTRODUCTION

The increased data rate and quality of service for end users have been greatly improved with the recent advent of technologies in the field of wireless communication. This has induced heavy network traffic and drop in data rate, hence the fifth-generation (5G) communication systems have been introduced amidst the surge in network and data traffic [1]. Due to its ability to offer a wider frequency spectrum and higher data rates of up to several GigaBites per Second, 5G wireless technology has been a revelation in the modern wireless communication domain. n78 (3.3–3.6 GHz), commonly known as sub-6 GHz band and offering a faster data rate than the 4G LTE (Long Term Evolution) frequency band, is one of the additional bands allocated for 5G communications in addition to the already existing fourth generation (4G) band. Also, the 5G communication network is crucial for the Internet of Things (IoT) because these devices need a higher data rate to function. This brings an increased demand for small-sized antennas with an enhanced bandwidth enough to support IoT devices [2].

The enhanced Mobile Broadband (eMBB) is considered as a critical component in the fifth-generation communication system. In comparison to earlier generations, the 5G network will be able to offer better data rates, capacity, and coverage, thanks to the implementation of eMBB. In essence, eMBB is a more sophisticated variation of 4G broadband [3]. Mobile broadband development is ensured by the implementation of the 5G New Radio (NR), a unified and more complex radio interface. In addition to the current 4G LTE frequency spectrum, the 5G NR global standard specifies additional mmWave band frequency ranges (3.5, 26, 28, and 40 GHz). Adaptive bandwidth technology with great spectrum flexibility has been used to provide a ubiquitous connection for a variety of applications [2]. The 5G communication infrastructure would consequently need to offer extraordinarily high bandwidth, ranging

Received 8 March 2023, Accepted 12 April 2023, Scheduled 24 April 2023
* Corresponding author: Madhusudhanan Nair Ayyappan (ayyappan995@gmail.com).
The authors are with the Department of Electronics and Communication Engineering, National Institute of Technology, Goa 403401, India.

from below 1 GHz to 100 GHz, depending on the implementation. As a result, there is a desire for small, affordable antennas that can operate over a variety of frequencies. The antenna described in this study maintains good gain and radiation efficiency while covering the whole high-frequency spectrum of the 5G NR global standard. Due to the increased spectrum availability, 5G radio technology becomes a key IoT enabler by supporting high traffic growth and the expanding need for high-bandwidth connections [4]. The Internet of Things connects technological advancements with practical business uses. IoT devices can communicate with one another in real-time because of 5G's broad coverage, low latency, and fast connectivity. As a result, this revolutionary technology will soon be used for a variety of industrial applications [5, 6]. The recommended Super Wide Band (SWB) antenna is a strong competitor in this regard due to its small size and ability to function in the mmWave frequency [7].

In the past few years, several works were carried out in the area of SWB antennas [8]. In [9], Azeem et al. proposed a low profile design with modified bow-tie shaped patch and two asymmetrical ground planes, but it does not support the super-wideband frequency range where as in [10], SWB technology is merged with the wearable textile technology to develop a novel fractal textile antenna to produce an impedance bandwidth of 1.4–20 GHz. A hexagonal Sierpinski antenna loaded with Sierpinski square slots is designed in [11] for super-wideband applications.

Coplanar waveguide is one of the effective feeding mechanism which helps in achieving impedance matching across a broad frequency range. A clown shaped radiator with a combination of ellipse, rectangle, and triangle is designed and prototyped in [12]. Some of the other super-wideband coplanar waveguide (CPW) antennas such as modified star-shaped fractal, Phi-shaped monopole, and triangular fractal are listed in [13–15], respectively. A loop-loaded bow-tie is employed with loop directors to enhance the gain, and this design with an impedance bandwidth of 13 : 1 at the same time is discussed in [16]. In [17, 18], an octagonal ring-shaped monopole antenna and hexagonal-shaped SWB antenna are proposed respectively to enhance the super-wideband characteristics of the antenna.

[19] offers a three-dimensional super-wideband antenna that is compact and has filtering capability. To obtain super-wideband performance, a conventional rectangular patch antenna has been altered by truncating the corners with semi-circles and using a partial ground plane with a trapezoidal shape.

This paper proposes a novel nature-inspired Turbinella geometry [21] which has not been explored so far. The shape of the Turbinella itself reveals that it is capable to produce an omnidirectional radiation pattern which is preferred for several next-generation applications. Moreover, the authors propose a new fractal concept that can evolve as a novel idea for obtaining a super wideband response. A mathematical analysis of fractal length and the effective area has been provided to validate the performance of the Turbinella-shaped fractal. The proposed antenna is derived from a conventional semi-circular monopole antenna. To obtain wide bandwidth and matching, a conventional semi-circular monopole antenna has been modified by a repetitive fractal arrangement of semicircular slots of depreciating dimensions on each line of the radiator which is yet to be explored in the antenna society. Further, the aid of a tuning-shaped defective ground plane structure has enhanced the super wideband characteristics of the antenna.

To the best of the authors' knowledge, the novelty of this work is that the size of the whole antenna is extremely compact for the working frequency range of 3–41.97 GHz. Furthermore, to highlight the novelty in the proposed work, the comparison of the proposed antenna with existing literature that operates in the same frequency range has been performed. The proposed design has achieved a compactness of over 81% with respect to the measured lower frequency, which is higher than the existing designs. Moreover, the most optimized compact size is realized with the maximized achievable bandwidth and is verified using the fundamental dimension limit theory proposed by Chu [22] and Mclean [23] which has not been explored in other designs in the literature. The antenna can be used for high data rate IoT applications and can also accommodate 5G millimeter wave bands. The simulation results were obtained using the CST (v2019) simulator software, which is based on the Finite Integration Technique (FIT). They were well validated by the experimental data.

2. A NOVEL TURBINELLA SHAPED MONOPOLE ANTENNA (TSMA) AND ITS WORKING MECHANISM

This section showcases the design of the Turbinella-shaped monopole antenna configuration and its super wideband behavior. The geometrical structure and dimensions of both the semicircular fractal and modified Turbinella patch are shown in Figs. 1(b)–(e), respectively. Fig. 1(b) shows the physical dimensions and structure of the proposed semicircular fractal antenna. Fig. 1(c) depicts the Defected Ground Plane (DGS) structure along with a tuning fork-shaped slot. Fig. 1(e) shows the structure of the modified TSMA. It has a symmetrical structure with respect to its longitudinal direction. In this design, Roger's RT Duroid laminate ($\epsilon_r = 2.2$, loss tangent, $\tan\delta = 0.0009$) is chosen for its exceptionally high-frequency qualities as well as its ability to endure frequency and temperature variations. The antenna is mounted on a substrate with a size of 32 mm × 25 mm ($0.32\lambda \times 0.25\lambda$), where λ is calculated with the measured $f_L = 3$ GHz. It is noted that the DGS structure used is the same for both the semicircular fractal and modified Turbinella patch.

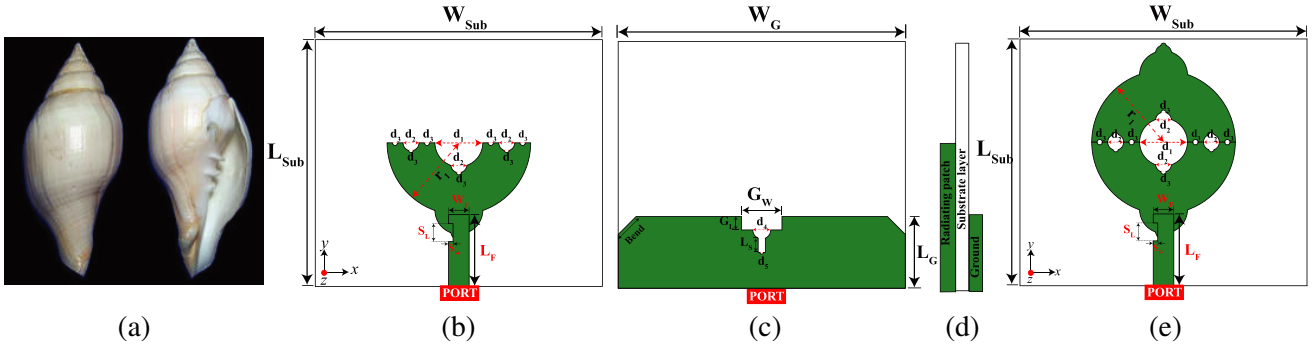

Figure 1. (a) Turbinella pyrum [21], semicircular fractal monopole antenna. (b) Front view. (c) Rear view. (d) Side view. (e) TISC monopole antenna front view; $L_{Sub} = 27.5$ mm, $W_{Sub} = 32$ mm, $L_F = 6.5$ mm, $W_F = 2.29$ mm, $L_G = 8$ mm, $G_W = 4.5$ mm, $G_L = 1.5$ mm, $r_1 = 8$ mm, $d_1 = 5.33$ mm, $d_2 = 1.77$ mm, $d_3 = 0.59$ mm, $d_4 = 2$ mm, $L_S = 1.58$ mm, $W_S = 0.80$ mm, $S_L = 2$ mm, $S_W = 0.5$ mm, Bend = 2 mm.

Perturbations in the patch and ground plane are critical for increasing the antenna's bandwidth. A novel modified semicircular fractal patch is incorporated on top of the substrate with a 50 Ω tapered microstrip feedline to enhance the antenna parameters and helps in the frequency tuning for super wideband operation. A defected ground plane with a tuning fork-shaped slot is mounted on the other side of the substrate. The tuning fork-shaped DGS structure on the ground plane plays a vital role in achieving enhanced bandwidth. This DGS structure ensures the electromagnetic coupling between the monopole antenna and the ground plane hence improving the bandwidth. By embedding the tuning fork-shaped slots on the ground plane, the model's effective capacitance and inductance are modified, causing the resonance frequency to shift towards the lower side, hence helping in achieving the compactness of the antenna. The 45° corner truncations (Bend) on both edges of DGS help in shifting the higher resonant frequency towards the right by exciting additional resonances. The optimized dimensions for the proposed antenna are provided in Fig. 1.

3. FUNDAMENTAL LIMITATION THEORY FOR ELECTRICALLY SMALL ANTENNAS

An electrically small antenna is often represented in terms of the antenna's radian length, $l = \frac{\lambda}{2\pi}$, and the highest possible dimension of the antenna, 'a'. Hence, an electrically small antenna can be expressed in terms of the inequality shown in [22].

Chu introduced the following expression of Q [22] for the lowest transverse magnetic (TM) mode:

$$Q = \frac{1 + 3k^2a^2}{k^3a^3[1 + k^2a^2]} \tag{1}$$

For lower values of ka (high Q), the two expressions are similar, but they start to diverge as ka approaches its upper limit (i.e., as it approaches 1).

As $ka \ll 1$, the equation becomes

$$Q \cong \frac{1}{k^3a^3} \tag{2}$$

According to this correlation, decreasing the antenna size causes a rapid rise in Q values, which in turn causes the bandwidth to be reduced. Being able to reduce size while improving bandwidth is therefore a crucial issue for electrically small antennas.

In [23], McLean introduced a new method for computing the antenna quality factor. This technique, in contrast to Chu's approximate equation, provides an accurate expression for Q calculation. At higher Q levels, this equation agrees with Chu's hypothesis, but at lower Q values, the two ideas diverge dramatically. The following are McLean's Equations for calculating Q [23].

$$Q = \frac{1}{k^3a^3} + \frac{1}{ka} \tag{3}$$

There is yet to be a standardized approach for determining the electrical size of broadband small antennas. Classical theories can be used to evaluate the narrow band antennas with fractional-bandwidth definitions and are not very effective for ratio or octaval bandwidth. However, the Chu and McLean theories' concepts can be used to find the best antenna sphere size (electrical size) that approaches the fundamental limitation theory. When the wideband antenna wavenumber is computed, the lower-bound frequency of the operating band is taken into account.

4. PARAMETRIC STUDY OF THE PROPOSED STRUCTURE

This section optimises each parameter of the proposed antenna by changing one parameter while holding the others constant. Parametric analysis is carried out for the DGS and feed section of the proposed structure. DGS is primarily employed to modify the antenna's surface current distribution. The inductance and capacitance of the feed line will alter because of these perturbations. The introduction of a rectangular defect into the ground plane results in an increase in parasitic capacitance as well as an increase in the fringing electric field and effective inductance. This parasitic capacitance improves the coupling between the ground and feed resulting in the enhancement of bandwidth.

The parametric analysis is initially performed for the DGS structure. The parametric values of slot1 (first rectangular slot) with dimension $G_L \times G_W$ are tailored in such a way as to enhance the bandwidth. By iterating through different positions and varying distances from the patch's centre, the slot's position has been improved to provide a broader bandwidth and better impedance matching. The values of G_L are varied from 1 mm to 3 mm. It is noted that the impedance bandwidth is better at 2 mm than 1 mm and 3 mm. An overall bandwidth of 23.11 GHz (4.20–27.31) is achieved with a notched band at 7.2 GHz as illustrated in Fig. 2(a). Similarly, G_W is varied from 2.5 mm to 4.5 mm in steps of 1 mm. Fig. 2(b) reveals that at 3.5 mm, the bandwidth is further enhanced to 24.39 GHz (3.74–28.13 GHz). With the introduction of slot 1, the effective inductance varies significantly resulting in the increase of parasitic capacitance which in turn improves the bandwidth.

Further, a semicircular slot (slot 2) with diameter d_4 is etched beneath the rectangular slot (slot 1). It is noted that effective inductance varies significantly with the introduction of a semicircular slot. Consequently, increasing the effective capacitance results in the enhancement of bandwidth. In this design, d_4 is varied from 1 mm to 3 mm, in which 2 mm shows better bandwidth enhancement than others and is depicted in Fig. 2(c). The bandwidth is slightly improved to 25.07 GHz (3.71–28.78 GHz) with the notched band inching closer to -10 dB.

Additionally, a rectangular slot (slot 3) with dimensions $L_s \times W_s$ is etched to improve the matching, thereby enhancing the bandwidth of the antenna. L_s is varied from 0.6 mm to 2.6 mm in steps of 1 mm keeping W_s fixed at 0.80 mm. This slot is intended to bring the notch at 7.2 GHz below -10 dB with a slight improvement in the impedance bandwidth to 25.52 GHz (3.58–29.1 GHz) as shown in Fig. 2(d). In addition to this, corner truncations are introduced to the DGS on both edges. This truncation shifts the resonance towards the higher frequency side resulting in the wider impedance bandwidth of 29.39 GHz (3.52–32.91 GHz). The optimized results are obtained for bend = 2 mm which is inferred from Fig. 2(e).

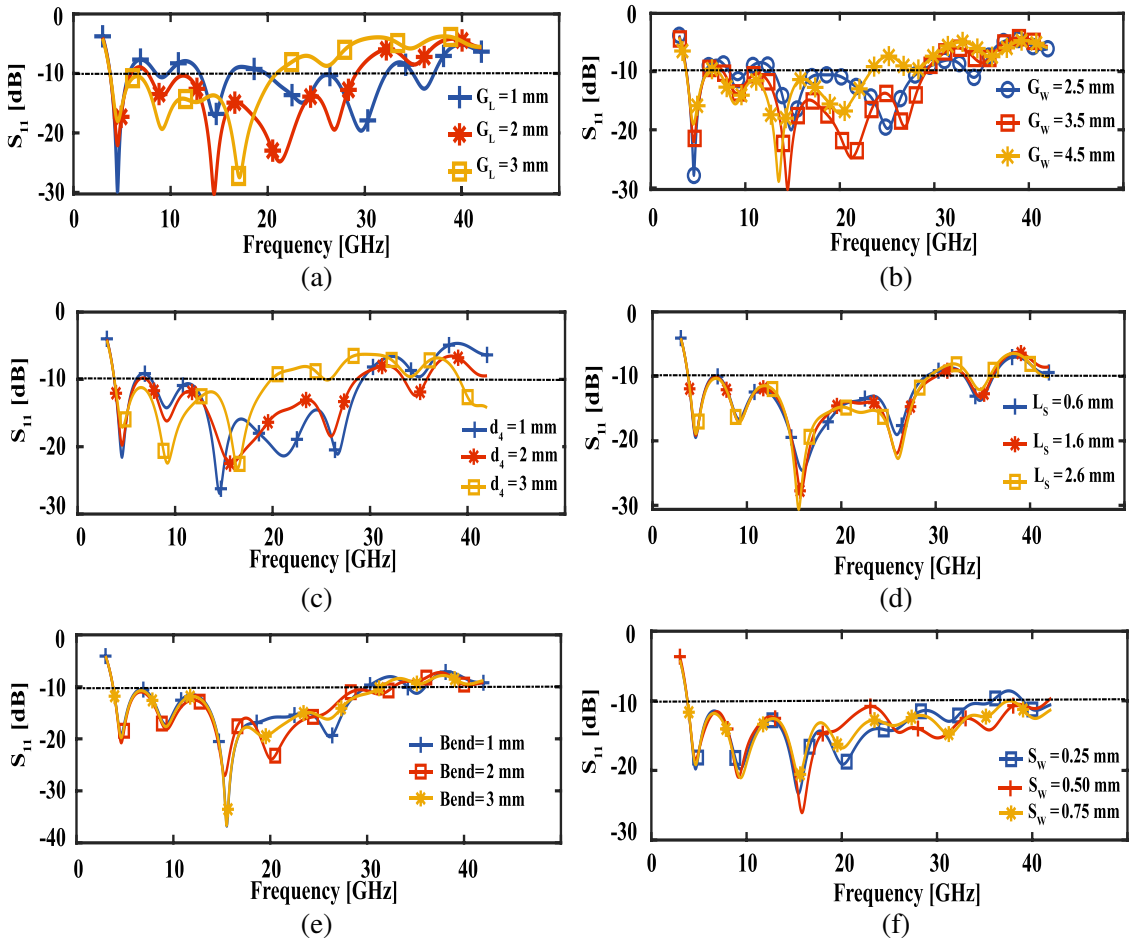

Figure 2. Variation of S_{11} for different values of (a) G_L, (b) G_W, (c) d_4, (d) L_S, (e) bend, (f) S_W.

In order to achieve the criteria for super wideband antenna ($f_H : f_L = 10 : 1$), a tapering is introduced to the microstrip feed network. Consequently, the quality factor gets decreased and results in wider impedance bandwidth. Moreover, tapering improves the coupling between the patch and the ground plane by introducing more overlapping areas between them. Here, a rectangular slot ($S_L \times S_W$) is introduced to enhance the super wideband characteristics. As a result, the bandwidth is greatly improved to 38.26 GHz (3.41–41.67 GHz) with a bandwidth ratio of 12.21 : 1 as illustrated in Fig. 2(f).

5. FRACTAL LENGTH ANALYSIS

Fractal antennas have two properties: infinite complexity and self-similarity, making them an excellent choice for wideband applications [25]. The fractal's infinite complexity and detailing properties aid in the miniaturization of the antenna structure, while the self-similarity property aids in the creation of additional resonances.

With the introduction of a fractal, the current length tends to increase, and the area tends to decrease with each iteration. This hence results in the broadening of bandwidth. Hence, the mathematical analysis of fractal length and effective area is very much critical in the development and design of fractal antennas. In this design, a novel fractal idea is employed on the semicircular patch. The evolution of the proposed antenna structure is shown in 5 stages as shown in Figs. 3(a)–(e). In stage-I, the design begins with an initiator (semicircular patch) with a diameter r as shown in

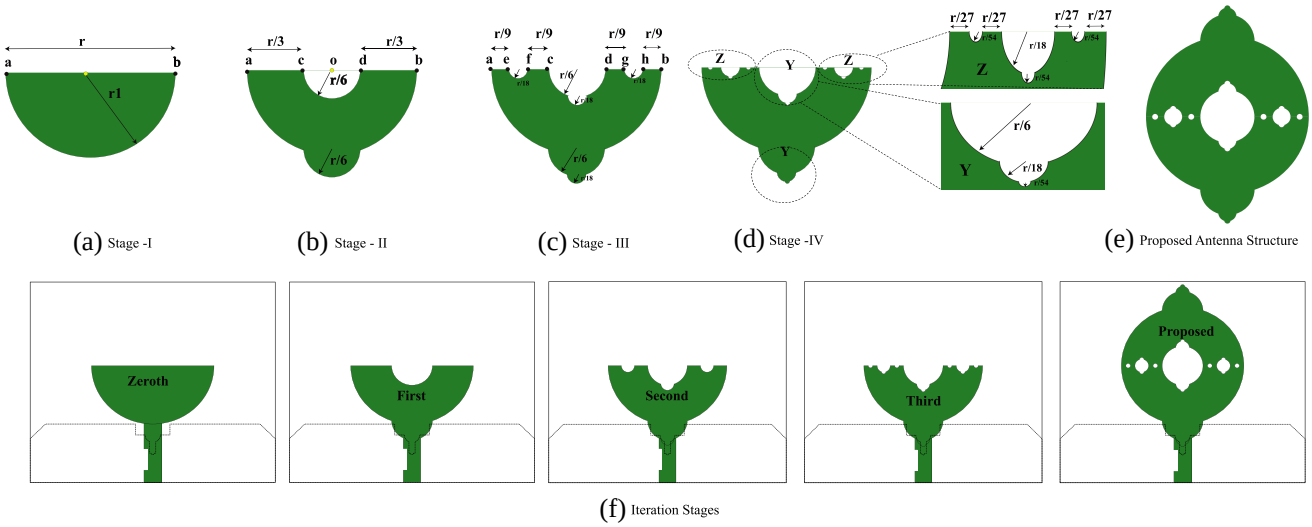

Figure 3. (a)–(e) Design stages of the fractal (f) iteration stages of the proposed antenna.

Fig. 3(a). The fractal length after the zeroth iteration will be:

$$fl_0 = \pi \times \frac{r}{2} + r \tag{4}$$

Stage II is composed of two design steps: (i). the diameter line 'ab' of the initiator is divided into three equal parts $ac = cd = db$, and then the initiator is modified by etching a semicircle of diameter $r/3$ from the center o of the patch; (ii). a semicircle of diameter $r/3$ is added simultaneously to the center of circumference as illustrated in Fig. 3(b). Therefore, the fractal length after the first iteration can be calculated as:

$$fl_1 = \pi \times \frac{r}{2} + 2 \times \pi \times \frac{r}{6} + r - 2\frac{r}{3} \tag{5}$$

Further, in stage III, semicircles of diameter $r/9$ are etched from the line segments ac and db, respectively, and a semicircle of diameter $r/9$ is added to the circumference of the previously etched semicircles as depicted in Fig. 3(c). Consequently, the effective current length or fractal length during the second iteration is:

$$fl_2 = \pi \times \frac{r}{2} + 2 \times \pi \times \frac{r}{6} + 4\pi\frac{r}{18} + r - \left[2\frac{r}{3} + 4\frac{r}{3^2}\right] \tag{6}$$

Similarly in stage IV as showcased in Fig. 3(d), semicircles with diameters $r/27$ are etched out from the line segments ae, fc, dg, and hb, respectively, and the semicircles with diameters $r/27$ are added to the circumference of the former. Hence, the fractal length evaluated for stage IV is shown below.

$$fl_3 = \pi\frac{r}{2} + 2\pi\frac{r}{6} + 4\pi\frac{r}{18} + 8\pi\frac{r}{54} + r - \left[2\frac{r}{3} + 4\frac{r}{3^2} + 8\frac{r}{3^3}\right] \tag{7}$$

Hence, the effective fractal length for the proposed design can be generalized as:

$$\Longrightarrow fl_n = r + \sum_{n=1}^{\infty}\left(\frac{2}{3}\right)^n r\left(\frac{\pi}{2} - 1\right) \tag{8}$$

Figure 3(e) shows the proposed TSMA, and it is obtained after concatenating stage IV and the mirror image of stage IV. With this process, symmetry and self-similarity are achieved for the proposed design. The structure in Fig. 3(e) resembles to a Turbinella hence named Turbinella shaped fractal. Hence, the effective fractal length for the proposed structure is computed as:

$$fl_{\text{proposed}} = 2\left[\pi\frac{r}{2} + 2\pi\frac{r}{6} + 4\pi\frac{r}{18} + 8\pi\frac{r}{54} + r\right] \tag{9}$$

where r = diameter of the initiator, fl_n = fractal length for n^{th} iteration; n = 0, 1, 2, 3 for zeroth iteration, first iteration, second iteration, and third iteration, respectively, fl_{proposed} = fractal length for the proposed design.

As the fractal design focuses on achieving compactness in design, it is very much important to calculate or analyze the area of the proposed fractal. The reduction in an area with the aid of the proposed fractal is analyzed for each iteration below. Similarly, with the same process used in computing the fractal length, the effective area is generalized as:

$$a_e = \frac{\pi r^2}{8}\left(1 - \sum_{n=1}^{\infty} \frac{2^n - 2}{3^n}\right) \tag{10}$$

The corresponding fractal length and variation in effective length after each iteration are validated in Table 1. From Table 1, it is understood that when the iteration stage proceeds from 0 to the proposed, there is a fractal length enhancement of 361.77%.

Table 1. Fractal length and area computation for each iteration with stage-wise bandwidth.

Iteration	**F.L (mm)**	**E.A ($\mathbf{mm^2}$)**	BW [GHz]	% BW
Iteration 0	16.56	25.13	8.07–15.15	60.9
Iteration 1	23.61	25.13	5.71–34.52	142.94
Iteration 2	25.65	24.5	5.54–35.10	145.47
Iteration 3	27	22.84	5.50–40.72	152.40
Proposed	76.47	48.61	3.41–41.67	169.74

This proposed fractal is evaluated for four iterations and one final symmetrical structure. The different stages of the TSMA antenna are illustrated in Fig. 3. Fig. 4(a) depicts the variations in the S_{11} parameter after each iteration stage of the TSMA. During the zeroth iteration, the antenna provides a bandwidth of 7.07 GHz (8.07–15.15 GHz) with a center frequency of 11.61 GHz as indicated in Fig. 4(a). From the figure, it is revealed that the impedance bandwidth of the initiator is mismatched at 15.15 GHz. As it progresses to the first iteration, a bandwidth of 28.61 GHz ranges from 5.71 GHz to 34.32 GHz with a center frequency of 20.01 GHz. The first iteration is marked with square markers, and it is evident from the figure that with the increase in the number of iterations, the resonant frequency gets shifted towards the lower side. The $*$ and $\circ$ markers in Fig. 4(a) depict the second and third iterations. From the figure, it is revealed that an impedance bandwidth of 29.56 GHz (5.54–35.10 GHz) and 35.22 GHz (5.50–40.72 GHz) is achieved for the second and third iterations, respectively. Further increase in the number of iterations may cause complexity in prototype manufacturing. But it is noted that the design was still not able to achieve super-wideband properties after the three iterations, i.e.,

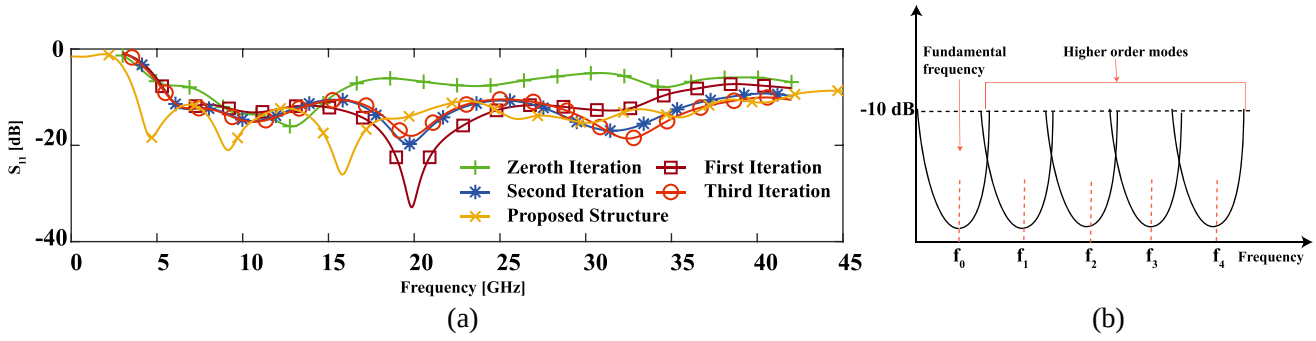

Figure 4. (a) Simulated S_{11} vs frequency plot for different iteration stages. (b) Overlaying of additional resonances to generate SWB.

ratio bandwidth. Hence, a symmetrical structure is employed not only to achieve super wideband characteristics but also to achieve omnidirectional radiation properties as shown in Fig. 3(f). This proposed structure resulted in a wider bandwidth of 38.26 GHz (3.41–41.67 GHz) and resonant shifting of the frequency. The comparison of bandwidths after five stages is tabulated in Table 1. The increased capacitive loading effect provided by the slots is responsible for the enhanced bandwidth. So these slots made on the patch and DGS are responsible for creating additional harmonics. The first resonance is calculated based on the initial dimension of the semicircular radiator. Additional resonances created there will be integral multiples of the first resonance. Fig. 4(b) depicts the proposed SWB antenna's operating mechanism. Neighboring resonances involving the fundamental and higher-order modes are overlapping here. This overlap of numerous resonances results in the super-wideband behavior.

6. EVALUATION OF SWB ANTENNA ELECTRICAL SIZE

The wavelength of an antenna's working frequency (λ) is used to calculate its size or dimensions [24]. The wavelength for the center frequency (λ_c) is often taken into account when the electrical size of a narrow-band antenna is determined, but this is not the case for UWB/SWB antennas. The wavenumber for the antenna's center frequency ($k = 2\pi/\lambda_c$) is used in classical fundamental limitation theories. As a result, these concepts work best in the development of narrow-band antennas, where the wavelength difference between the center and edge frequencies is significantly smaller [6].

However, a close inspection of the UWB/SWB antenna's wavelengths for various operating frequencies indicates that the center frequency wavelength is notably different from the lower and upper bound wavelengths. As a result, for UWB/SWB antennas, employing the center wavelength directly for the entire range of frequencies is not feasible. A more acceptable way is to define the antenna electrical size to satisfy the equation $k_L a = 1$, where k_L is the wavenumber that corresponds to the lower bound frequency of the bandwidth. The electrical size calculation of the proposed SWB antennas is tabulated in Table 2.

In Fig. 5(a), the quality factor, the Q of antennas, both simulated and manufactured, is plotted against their electrical sizes, and the findings are compared to Chu and McLean's theoretical fundamental dimension limit curves. It should be noted that the proposed antenna agrees well with

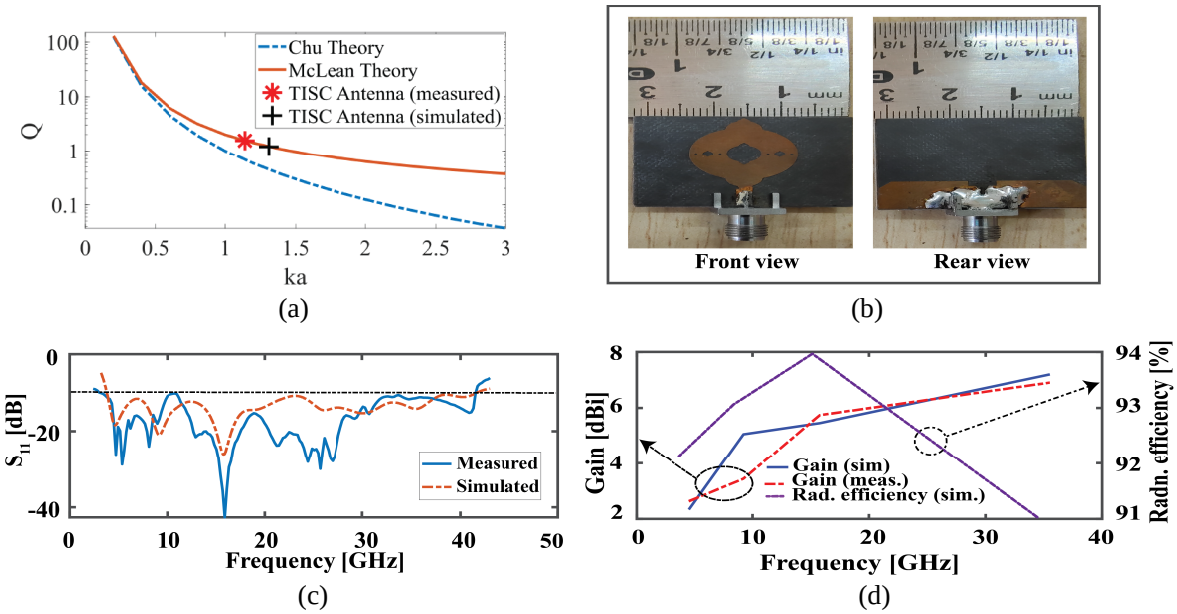

Figure 5. (a) Comparison of proposed SWB antennas (simulated and fabricated) with the theoretical dimension limit curves. (b) Fabricated prototype of the proposed antenna. (c) Measured and simulated S_{11} plots. (d) Measured gain and simulated gain and radiation efficiency plots for the proposed antenna.

Table 2. Electrical size calculation of proposed SWB antennas.

Patch Height (mm)	f_L **(GHz)**	**Wavelength at** λ_L **(mm)**	**Wave Number** (k_L)	$k_L a$ **(rad)**
0.035	3 [fabricated]	100	0.0628	1.067
0.035	3.41 [simulated]	87.97	0.0714	1.21

McLean's curve of the fundamental dimension limit theorem, which is used to calculate the quality factor of the proposed antenna using McLean's equation. As a result, it can be concluded that the proposed super-wideband antenna was designed in close accordance with the fundamental dimension limit theorem [24].

7. RESULTS AND DISCUSSION

In order to validate the simulation results, the proposed miniaturized antenna, TSMA, was manufactured using the Leiterplatten-Kopierfrasen (LPKF) printed circuit board (PCB) prototyping machine, and antenna parameters such as return loss, radiation pattern, and gain were measured using a Keysight PNA Network Analyzer (10 MHz–43.5 GHz). Fig. 5(b) shows the fabricated prototype of the proposed antenna. The simulated and measured return losses for $S_{11} \leq -10$ dB against frequency are plotted in Fig. 5(c). A fractional bandwidth of 173.33% [3–41.97 GHz] and 169.74% [3.41–41.67 GHz] is achieved in fabrication and simulation, respectively. The variations in simulated and measured results might be due to fabrication inconsistencies. Fig. 6 shows the Vector Network Analyzer (VNA) measurement setup.

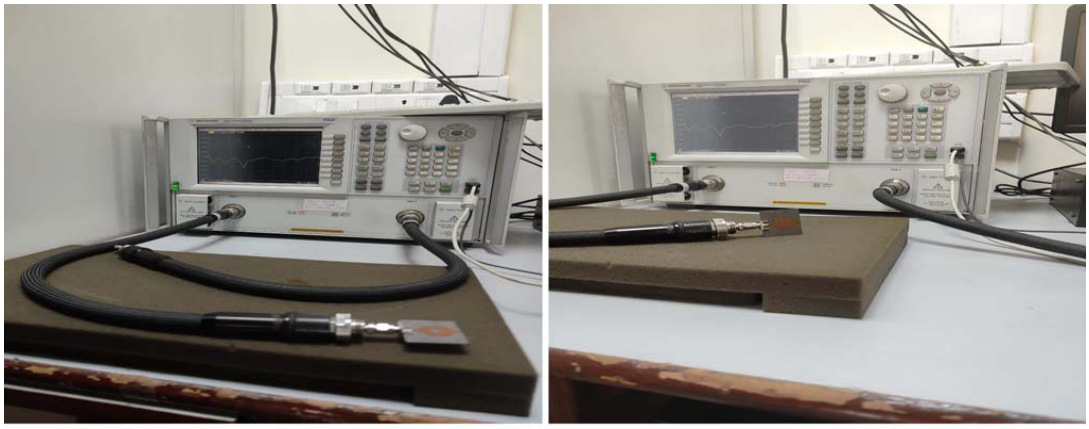

(a) (b)

Figure 6. VNA measurement setup.

7.1. Gain and Radiation Efficiency

The proposed antenna's simulated and measured broadside gains are shown in Fig. 5(d). It is clear from Fig. 5(d) that the gain increases with the rise in frequency. As a result, the antenna's effective aperture increases in proportion to the wavelength. The gain has become flat and slightly dropped at the mid-frequency range. This is because the current intensity increases with respect to frequency at the sharp edges of the structure, which creates delay paths in the antenna. The simulated and measured gains at the second resonance differ by 1.32 dBi due to SubMiniature version A (SMA) connector loss and fabrication tolerances [26, 27].

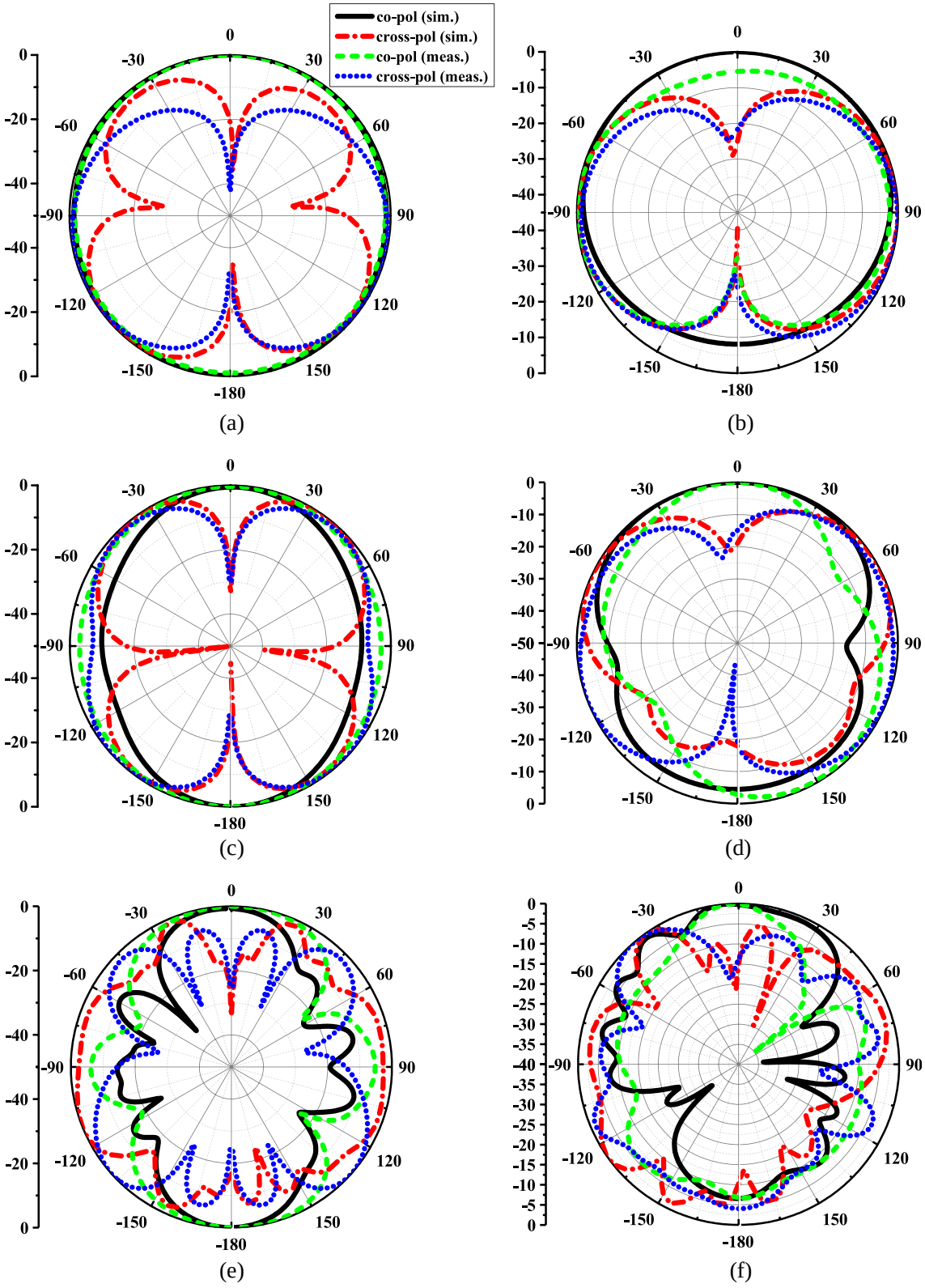

Figure 7. 2-D radiation pattern, (a) E-plane at 4.55 GHz, (b) H-plane at 4.55 GHz, (c) E-plane at 9.22 GHz, (d) H-plane at 9.22 GHz, (e) E-plane at 35.53 GHz, (f) H-plane at 35.53 GHz.

The measured peak gain is 6.92 dBi at 35.51 GHz as depicted in the graph. It is observed from Fig. 5(d) that the radiation efficiency increases with respect to the rise in frequency, and maximum efficiency about 94.3% is reported at 15.75 GHz and lies within 91% throughout the frequency of operation.

7.2. Radiation Pattern and Current Distribution

Figure 7 shows the 2-D radiation patterns of the antenna. The far-field pattern has omnidirectional radiation characteristics for lower frequencies such as 4.55 GHz and 9.22 GHz. Moreover, at high frequencies, the radiated power is dispersed across the top and bottom sides of the antenna. Unfortunately, the antenna's radiation is attenuated in the front and back sides indicating minimal distortion in those areas, hence resulting in a deviated omnidirectional radiation pattern. The acceleration of charges or varying currents contributes to the fundamental mechanism for antenna's radiation. To permit current distribution over a larger frequency range, the proposed TSMA operates in a hybrid mode of standing and traveling waves at higher frequencies. Fig. 8 shows the radiation pattern measurement setup. Current distributions at different frequencies are illustrated in Figs. 9(a)–(c). So, the feed line's presence of a significantly greater amount of current provides insight into the mode variation. First order harmonic resonance is observed at 4.55 GHz. From Fig. 9(a), it is apparent that the current propagates along the tapered feed and the lower half of the Turbinella radiator. As shown in Fig. 9(a), this results in a standing wave with a significant envelope bump. A current null is generated around the central fractal slot. Hence, the radiation pattern in Fig. 7(a) is donut shaped with minimum radiation from the antenna's top side.

Since there is an accumulation of current along the bottom side of the Turbinella radiator, the radiated power is mostly confined to the front side of the antenna. According to the current distribution at 9.22 GHz, the higher-order modes arise as the frequency increases. At this frequency, the second-order harmonic is discernible, and the current distribution is primarily centred close to the lower part of the radiating patch. Moreover, as depicted in Fig. 9(b), the current also extends along the upper angular

(a) (b)

Figure 8. Radiation pattern measurement setup in anechoic chamber (a) *E*-plane, (b) *H*-plane.

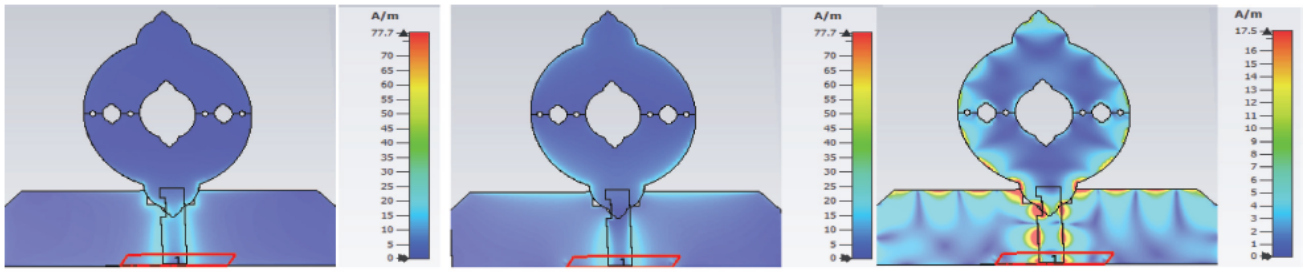

(a) (b) (c)

Figure 9. Current distribution at (a) 4.55 GHz, (b) 9.22 GHz, (c) 35.53 GHz.

parts of the radiating patch. This propagation causes a standing wave to develop around the top of the perturbing slots of the radiator. This standing wave causes a radiating null at the antenna top, just as it did with the first resonant frequency at 4.55 GHz. In this case, the antenna's far-field pattern still displays a donut structure with the bulk of the radiated power accumulating around the top side and front side of the Turbinella antenna.

Moreover, when the frequency rises, higher-order harmonics increase as well, creating a complex distribution along the antenna structure. This distribution causes the TSMA to function in a hybrid mode that combines standing and travelling waves, and travelling wave is considered as the most vital factor. Yet, as seen in Fig. 9(c), a standing wave is generated around the center slots and Turbinella radiator. As a result, there is a significant amount of current null on the radiator surface since the current primarily passes through various distributed locations on the radiator's edges. This gives insight into the deteriorated radiation pattern at 35.53 GHz, as seen in Figs. 7(e) and 7(f). In addition, the radiated power gets suppressed in the front and rear sides of the patch. The far-field radiation is mostly formed by these radiating patch edges, resulting in a distorted omnidirectional pattern, as shown in Fig. 7(e) and Fig. 7(f) [7]. The ground plane contribute at higher frequencies, as we can see from the current distribution, but the feedline and radiator edges account for the most of the power. As can be seen in Fig. 9(c) [28], the DGS has suppressed the surface currents on the patch antenna. Hence, these attributes of the antenna make it a good choice for high data rate IoT applications and millimeter-wave 5G applications. But at the same time, we were able to achieve a Cross-Polar Difference (XPD) level of ≥ 30 dB at both E-plane and H-plane at 35.53 GHz. Moreover, since the proposed antenna is a super wideband antenna, it also covers other applications in S (from 3–4 GHz), C, X, Ka, K, Ku, and Q bands.

7.3. Bandwidth Dimension Rate (BDR)

BDR is an important parameter of the super wideband antenna which draws the relationship between the compactness and bandwidth of the antenna. BDR signifies how much percentage bandwidth that an antenna can provide per unit electrical area and is mathematically defined as:

$$\mathrm{BDR} = \frac{\text{bandwidth}\%}{\lambda_{\text{length}} \times \lambda_{\text{width}}} \tag{11}$$

where λ_{length} and λ_{width} are the electrical length and width of the radiator, respectively, and λ is calculated with respect to f_L. From Equation (11), it is evident that the BDR for the proposed antenna is 2166.63 which is very much comparable with the antennas in the existing literature. Table 3 tabulates the comparison of the proposed antenna with the existing literature. From the comparison table provided below, it is understood that the proposed antenna has superior results in terms of bandwidth and ratio bandwidth to all the other designs operating in the similar frequency range.

8. TIME DOMAIN PERFORMANCE

The time domain analysis of the proposed antenna is analyzed to characterize the pulse-shaping properties of the antenna. In an ideal case, the shapes of the received pulse and transmitted pulse should be the same. However, for practical applications, the antenna should be designed in such way to avoid distortions in the form of a ringing effect. Hence, the time domain analysis of super wideband antenna is very much critical to corroborate the similarity of the receiving and transmitting pulses [30].

To perform the time domain analysis, two similar antennas are arranged in different configurations, (i) side by side and (ii) face to face. The distance between the antennas is calculated using the Fraunhofer's distance $r \leq \frac{2D^2}{\lambda}$, where r is the distance between the similar antennas, D the largest dimension of the radiator, and λ is calculated with respect to the lowest frequency. The two different time domain characteristic configurations, i.e., side-by-side and face-to-face configurations, are illustrated in Fig. 10(a). For both configurations, Gaussian pulse is employed for both transmission and reception. A crucial time domain metric, the fidelity factor (FF), which denotes the similarity between the transmitted and received waveforms, can be calculated with respect to Fig. 10(b). It is noticeable that each of the received pulses has a slight degree of ringing before the excitation starts due to channel

Table 3. Comparison of the proposed antenna with previously reported antennas in the literature.

Reference	Dimension [λ^2]	OFR [GHz]	% BW	RBW	BDR	Peak Gain [dBi]
[9]	$0.25\lambda \times 0.20\lambda$	3.035–17.39	140.56	5.72 : 1	2811	6.16 at 16.80 GHz
[10]	$0.28\lambda \times 0.285\lambda$	1.4–20	173.80	14.30 : 1	1677.90	-
[11]	$0.32\lambda \times 0.34\lambda$	3.4–37.4	166.67	11 : 1	1531.90	5.9 at 18 GHz
[12]	$0.27\lambda \times 0.28\lambda$	3.1–40	171.22	12.90 : 1	2267	6
[13]	$0.30\lambda \times 0.29\lambda$	4.6–52	167.49	11.30 : 1	1903.20	4 (Average Gain)
[14]	$0.28\lambda \times 0.234\lambda$	3.5–37.2	164	10 : 1	2541.2	13.7 dB at 33 GHz
[15]	$0.326\lambda \times 0.26\lambda$	3.06–35	168	11.43 : 1	1944.6	-
[16]	$0.32\lambda \times 0.32\lambda$	0.42–5.5	171.62	13 : 1	1676	7.96
[17]	$0.34\lambda \times 0.34\lambda$	2.59–31.14	169	12.02 : 1	1381.96	5
[18]	$0.4\lambda \times 0.4\lambda$	3.37–27.71	156.6	8.22 : 1	978.8	7.63 at 23.84 GHz
[19]	$0.20\lambda \times 0.19\lambda$	2.45–20	156.34	8.16 : 1	4114	-
[20]	$0.35\lambda \times 0.20\lambda$	3–35	168.42	11.6 : 1	-	11.2
[30]	$0.09\lambda \times 0.12\lambda$	6–25	122.58	4.16 : 1	-	7 at 25 GHz
[31]	$0.267\lambda \times 0.2\lambda$	2–25	168.42	11.6 : 1	-	11.2
[32]	$0.31\lambda \times 0.37\lambda$	3.1–10.6	109.48	3.4 : 1	954.5	6.3 at 12 GHz
[33]	$1.861\lambda \times 1.86\lambda$	3.5–5.5	48.8	1.57 : 1	14.10	8.6 dB at 4.3 GHz
Proposed	$\mathbf{0.32\lambda \times 0.25\lambda}$	**3–41.97**	**173.33**	**14 : 1**	**2166.63**	**6.92 at 35.51 GHz**

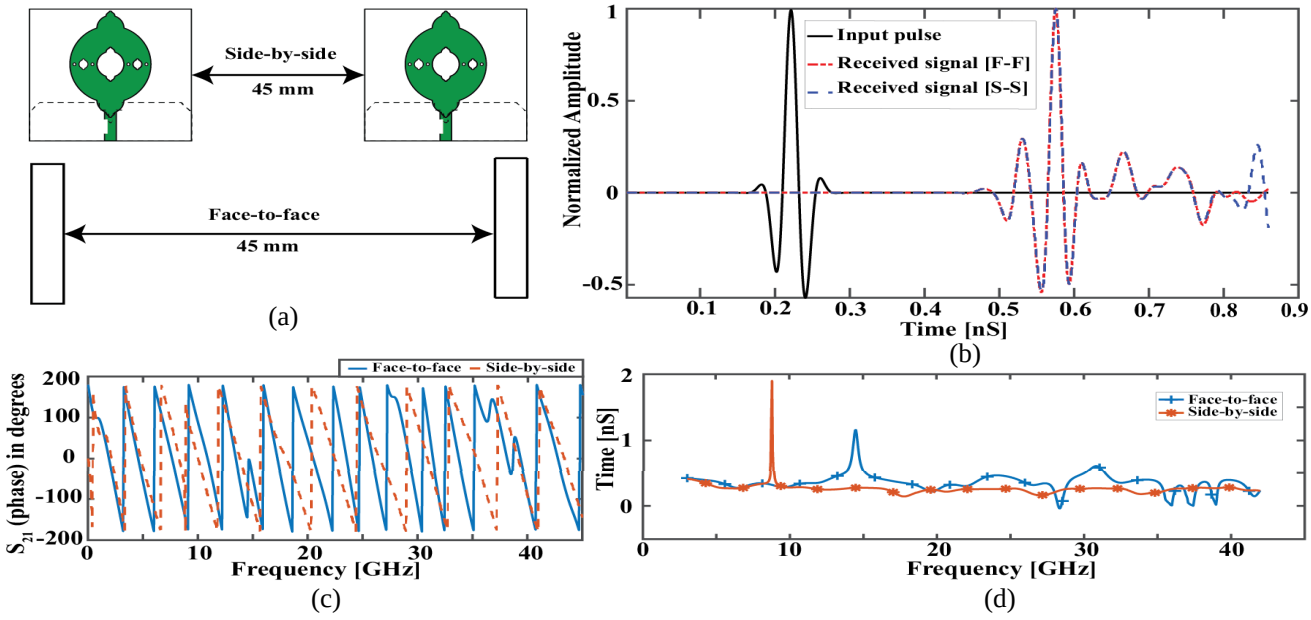

Figure 10. (a) Antenna arrangement for time-domain characterization. (b) Simulated normalized amplitude of input and received pulse. (c) Phase variation in face-to-face and side-by-side configurations. (d) Group delay vs frequency plot.

noise. As seen in Fig. 10(b), the pulse structure remains unchanged in both of the received pulses, indicating lossless reception of transmitted data.

$$\hat{T}_s(t) = \frac{T_s(t)}{\left[\int_{-\alpha}^{\alpha} |T_s(t)|^2 dt\right]^{1/2}} \tag{12}$$

$$\hat{R}_s(t) = \frac{R_s(t)}{\left[\int_{-\alpha}^{\alpha} |R_s(t)|^2 dt\right]^{1/2}} \tag{13}$$

The fidelity factor is given by

$$FF = \max \int_{-\alpha}^{\alpha} \hat{T}_s(t)\hat{R}_s(t+\tau)dt \tag{14}$$

$\hat{T}_s(t)$ denotes the transmitted pulse waveform, and $\hat{R}_s(t)$ denotes the pulse at receiving antenna port B. Apparently, the value of FF lies in between 0 and 1 because of normalization. The FF value of 1 indicates that the transmitted pulse and received pulse are identical, i.e., there is no signal lost during the transmission. On the other hand, the FF value 0 indicates that due to signal attenuation, the received pulse is not identical to the transmitted pulse. Hence, the closer value of FF towards 1 ensures minimum distortion to the received pulse [29].

The fidelity factor is analyzed for both side-by-side and face-to-face configurations in our paper. FF is 0.896 and 0.871 for side-by-side and face-to-face configurations, respectively. This implies that the received pulse is 89.6% similar to the transmitted pulse for side-by-side configuration, and in the case of face-to-face configuration, the received and transmitted pulses are identical, 87.1%.

8.1. Group Delay

Figure 10(c) represents the S_{21} phase variation for the two configurations. It should be noticed that the phase variation in both configurations is linear over the entire operating frequency, proving that the pulse being received contains no out-of-phase elements. Group delay, which is theoretically derived as the negative derivative of phase change with respect to frequency, is another crucial time domain characteristic. As a signal travels through a device, it experiences amplitude and phase distortion. A wave has multiple frequency components when it reaches a device's input. As a result, the group delay defines the input signal's average time lag at each frequency. It also indicates how widely dispersed the device is. In addition, group delay also validates the linear phase response across frequency of operation [29]. Group delay is minimum for side-by-side and face-to-face configurations, hence making it suitable for 5G millimeter wave applications as illustrated in Fig. 10(d).

9. CONCLUSION

A Turbinella-shaped monopole antenna is designed, analyzed, and validated for 5G millimeter wave applications. This proposed antenna structure achieves a BDR of 2166.63 which is very comparable with the existing literature and is suitable for IoT applications. The presented antenna provides an impedance bandwidth of 38.97 GHz (3–41.97 GHz) with a fractional bandwidth of 173.33% and ratio bandwidth of 14 : 1 and also achieves compactness of 81%. The measured gain of the proposed antenna is in the range of 2.4–6.92 dBi over the frequency of operation. Moreover, the most optimized compact size is realized with the maximized achievable bandwidth and is verified using the fundamental dimension limit theory proposed by Chu and Mclean which has not been explored in other designs in the literature. From the comparison table, it is observed that the proposed antenna has superior results to most of the literature and comparable results with the others. Considering these advantages, the proposed antenna finds its application in eMBB applications including 5G millimeter wave bands like n77, n78, and n258. Time domain analysis was used to assess the transient behavior of the proposed antenna for pulsed operations, confirming the antenna's suitability for a variety of wideband wireless applications.

ACKNOWLEDGMENT

The authors acknowledge the support of Science and Engineering Research Board (SERB), Department of Science and Technology (DST), Govt. of India, under project No. ECR/2017/003341. Authors also would like to thank Ravi Prasad K. Jagannath, Associate Professor, in the Department of Applied Sciences at the National Institute of Technology Goa, India for his guidance and support.

REFERENCES

1. Rappaport, T. S., Y. Xing, G. R. MacCartney, A. F. Molisch, E. Mellios, and J. Zhang, "Overview of millimeter wave communications for fifth-generation (5G) wireless networks — With a focus on propagation models," *IEEE Transactions on Antennas and Propagation*, Vol. 65, No. 12, 6213–6230, 2017.
2. Ancans, G., V. Bobrovs, A. Ancans, and D. Kalibatiene, "Spectrum considerations for 5G mobile communication systems," *Procedia Computer Science*, Vol. 104, 509–516, 2017.
3. Teyeb, O., G. Wikstrom, M. Stattin, T. Cheng, S. Faxer, and H. Do, "Evolving LTE to fit the 5G future," *Ericsson Technol. Rev.*, Vol. 95, No. 2, 8–22, 2017.
4. Dahlman, E., G. Mildh, S. Parkvall, J. Peisa, J. Sachs, and Y. Skold, "5G radio access," *Ericsson Rev.*, Vol. 6, No. 1, 1–12, Jun. 2014.
5. Young, L. J., "Telecom experts plot a path to 5G [news]," *IEEE Spectr.*, Vol. 52, No. 10, 14–15, Oct. 2015.
6. Ayyappan, M. and P. Patel, "On design of a triple elliptical super wideband antenna for 5G applications," *IEEE Access*, Vol. 10, 76031–76043, 2022.
7. Dey, S., M. S. Arefin, and N. C. Karmakar, "Design and experimental analysis of a novel compact and flexible super wide band antenna for 5G," *IEEE Access*, Vol. 9, 46698–46708, 2021.
8. Balani, W., M. Sarvagya, T. Ali, P. M. M. Manohara, J. Anguera, A. Andujar, and S. Das, "Design techniques of super-wideband antennas-existing and future prospective," *IEEE Access*, Vol. 7, 141241–141257, 2019.
9. Azim, R., M. T. Islam, H. Arshad, M. M. Alam, N. Sobahi, and A. I. Khan, "CPW-fed super-wideband antenna with modified vertical bow-tie-shaped patch for wireless sensor networks," *IEEE Access*, Vol. 9, 5343–5353, 2020.
10. Karimyian-Mohammadabadi, M., M. A. Dorostkar, F. Shokuohi, M. Shanbeh, and A. Torkan, "Super-wideband textile fractal antenna for wireless body area networks," *Journal of Electromagnetic Waves and Applications*, Vol. 29, No. 13, 1728–1740, 2015.
11. Singhal, S. and A. K. Singh, "CPW-fed hexagonal Sierpinski super wideband fractal antenna," *IET Microwaves, Antennas & Propagation*, Vol. 10, No. 15, 1701–1707, 2016.
12. Garg, R. K., S. Singhal, and R. S. Tomar, "A CPW fed Clown-shaped super wideband antenna," *Progress In Electromagnetics Research Letters*, Vol. 99, 159–167, 2021.
13. Singhal, S. and A. K. Singh, "Modified star-star fractal (MSSF) super-wideband antenna," *Microwave and Optical Technology Letters*, Vol. 59, No. 3, 624–630, 2017.
14. Singhal, S. and A. K. Singh, "CPW-fed Phi-shaped monopole antenna for super-wideband applications," *Progress In Electromagnetics Research C*, Vol. 64, 105–116, 2016.
15. Siahcheshm, A., J. Nourinia, Y. Zehforoosh, and B. Mohammadi, "A compact modified triangular CPW-fed antenna with multioctave bandwidth," *Microwave and Optical Technology Letters*, Vol. 57, No. 1, 69–72, 2015.
16. Ajith, K. K. and A. Bhattacharya, "A novel compact superwideband bowtie antenna for 420 MHz to 5.5 GHz operation," *IEEE Transactions on Antennas and Propagation*, Vol. 66, No. 8, 3830–3836, 2018.
17. Okan, T., "A compact octagonal-ring monopole antenna for super wideband applications," *Microwave and Optical Technology Letters*, Vol. 62, No. 3, 1237–1244, 2020.

18. Faouri, Y., S. Ahmad, S. Naseer, K. Alhammami, N. Awad, A. Ghaffar, and M. I. Hussein, "Compact super wideband frequency diversity hexagonal shaped monopole antenna with switchable rejection band," *IEEE Access*, Vol. 10, 42321–42333, 2022.
19. Agarwal, S., A. Sharma, I. J. Garcia Zuazola, and W. G. Whittow, "Three-dimensional miniaturized super wideband antenna with filtering capabilities," *International Journal of RF and Microwave Computer-Aided Engineering*, Vol. 32, No. 8, e23200, 2022.
20. Shahu, B. L., S. Pal, and N. Chattoraj, "Design of super wideband hexagonal-shaped fractal antenna with triangular slot," *Microwave and Optical Technology Letters*, Vol. 57, No. 7, 1659–1662, 2015.
21. Chandra Shekar, M., S. Arularasan, N. M. Nathani, G. U. Zaman, and C. G. Joshi, "Genetic architecture of three Turbinella pyrum varieties (Linnaeus, 1758) from the southeast coast of India," *Marine Ecology*, Vol. 37, No. 3, 588–598, 2016.
22. Chu, L. J., "Physical limitations of omni-directional antennas," *J. Appl. Phys.*, Vol. 19, No. 12, 1163–1175, 1948.
23. McLean, J. S., "A re-examination of the fundamental limits on the radiation Q of electrically small antennas," *IEEE Trans. Antennas Propag.*, Vol. 44, No. 5, 672, May 1996.
24. Dey, S. and N. C. Karmakar, "Design of novel super wide band antenna close to the fundamental dimension limit theory," *Scientific Reports*, Vol. 10, No. 1, 1–15, 2020.
25. Anguera, J., C. Puente, C. Borja, and J. Soler, "Fractal shaped antennas: A review," *Encyclopedia of RF and Microwave Engineering*, 2005.
26. Gauthier, G. P., A. Courtay, and G. M. Rebeiz, "Microstrip antennas on synthesized low dielectric-constant substrates," *IEEE Transactions on Antennas and Propagation*, Vol. 45, No. 8, 1310–1314, 1997.
27. Reniers, A. C., A. R. van Dommele, A. B. Smolders, and M. H. Herben, "The influence of the probe connection on mm-wave antenna measurements," *IEEE Transactions on Antennas and Propagation*, Vol. 63, No. 9, 3819–3825, 2015.
28. Ji, Z., G.-H. Sun, and H. Wong, "A wideband circularly polarized complementary antenna for millimeter-wave applications," *IEEE Transactions on Antennas and Propagation*, Vol. 70, No. 4, 2392–2400, 2022.
29. Balani, W., M. Sarvagya, A. Samasgikar, T. Ali, and P. Kumar, "Design and analysis of super wideband antenna for microwave applications," *Sensors*, Vol. 21, No. 2, 477, 2021.
30. Manohar, M., R. S. Kshetrimayum, and A. K. Gogoi, "Super wideband antenna with single band suppression," *International Journal of Microwave and Wireless Technologies*, Vol. 9, No. 1, 143–150, 2017.
31. Manohar, M., R. S. Kshetrimayum, and A. K. Gogoi, "Printed monopole antenna with tapered feed line, feed region and patch for super wideband applications," *IET Microwaves, Antennas & Propagation*, Vol. 8, No. 1, 39–45, 2014.
32. Kumar, A. L., A. Ranjan, M. Chauhan, V. K. Killamsetty, and B. Mukherjee, "Circular SRR shaped UWB antenna with WiMAX band notch characteristics," *2018 IEEE Radio and Antenna Days of the Indian Ocean (RADIO)*, 1–2, IEEE, 2018.
33. Gupta, S., M. Chauhan, and B. Mukherjee, "Fractal on hemispherical DRA by Descarte's circle theorem for wideband application," *2018 Conference on Information and Communication Technology (CICT)*, 1–6, IEEE, 2018.